29th EPS Conference on Plasma Phys. and Contr. Fusion Montreux, 17-21 June 2002 ECA Vol. **26B**, P-1.118 (2002)

Understanding Sawtooth Period Behaviour with Electron and Ion Cyclotron Resonance Heating and Current Drive

C. Angioni†, T.P. Goodman, M.A. Henderson, M.J. Mantsinen[1], O. Sauter

Centre de Recherches en Physique des Plasmas,
Association EURATOM - Confédération Suisse, EPFL, 1015 Lausanne, Switzerland
[1] *Helsinki University of Technology, Association EURATOM-Tekes, Espoo, Finland*
† Present address: *Max-Planck Institut für Plasmaphysik, IPP-EURATOM Association, D-85748 Garching bei München, Germany*

1. Introduction

Sawtooth activity has strong effects on plasma profiles and plasma performance. Sawtooth stabilisation, although favourable in producing peaked profiles, can create seed islands capable of triggering neoclassical tearing modes [1] and prevents the removal of impurities from the plasma core. Therefore the sawtooth period should play a non–negligible role in determining the plasma performance in a burning plasma and should be controlled during the reactor operation in order to maximize the fusion yield. For these reasons, the physical understanding of the sawtooth period behaviour must be considered of major importance, particularly in the presence of radiofrequency heating. This can indeed modify the local plasma parameters in such a way to allow the control of the sawtooth period [2, 3, 4, 5].

In particular in the present paper the sawtooth period responses to localized heating and current drive obtained in two different tokamaks, TCV and JET, and with two different auxiliary heating systems, electron cyclotron resonance heating (ECH) and ion cyclotron resonance heating (ICRH) respectively, are analyzed, compared and simulated with a sawtooth period model. This is done using the transport code PRETOR [6], including a sawtooth period model [7, 8] first introduced to predict the sawtooth period in a ITER burning plasma. This model provides sawtooth crash triggers from the linear stability thresholds of the internal kink in both ideal and non–ideal regimes and prescriptions for the post–crash relaxed profiles following the Kadomtsev complete reconnection model. The model was found consistent with the experimental behaviour in ECH discharges in TCV [9] and in NBI discharges in JET [10].

Recent new experimental results in TCV have motivated a set of simulations which clearly identify the separate effects of localized heating (Section 2) and current drive (Section 3) along the full plasma minor radius. It is shown that the effects so identified are consistent with the complex sawtooth period response observed in a JET discharge with ICRH and ICCD [5] as the resonance moves through the inversion radius (Section 4).

2. TCV ECH discharges: stabilisation and destabilisation with localized heating

The stabilizing effect of ECH close to the $q = 1$ surface was observed for the first time at our knowledge in Ref. [11] and the stabilizing location was roughly identified ouside the $q = 1$ surface. More recently, previous TCV experiments [3, 4], performing vertical sweeps of the ECH beam in the poloidal cross section, have pointed out that the sawtooth period (τ_{saw}) and amplitude strongly increase when the power deposition crosses a given flux surface, located very close to the $q = 1$ surface. The sawtooth period behaviour obtained in those experiments was found consistent with the simulations obtained applying the previously mentioned sawtooth period model [9]. In the simulations the radial position of the heating location maximizing τ_{saw} was found to be located just outside the radius ρ_1 of the $q = 1$ surface.

In the present work we show results obtained in recent shots in which the higher plasma current and the slow beam sweep in a very narrow plasma layer in the vertical direction allow us to more easily compare the inversion radius ρ_{inv}, experimentally identified with ρ_1, and the ECH deposition location, computed with the ray–tracing code TORAY–GA [12]. To obtain visible heating effects on τ_{saw} in the case of plasmas with higher Ohmic heating power density, it was necessary to apply three beams of 0.45 MW each, one on top of the other (limiter plasmas, $I_p = 350$ kA, $B_t = 1.45$ T, line averaged density $n_{el} = 1.6\ \ 10^{19}$ m^{-3}, $q_{edge} = 3$).

The results obtained in shot ♯21103 are shown in Figure 1. In Figure 1(a), circles show the evolution of τ_{saw} as a function of the power deposition. The power deposition is identified with the barycentre of the power density profile as computed with TORAY–GA. The normalized radial coordinate is $\rho = (V/V_{edge})^{1/2}$, where V is the volume enclosed by the corresponding flux surface. With triangles we have plotted τ_{saw} as computed by a PRETOR simulation performed using smoothed TORAY–GA power deposition profiles. The heating power density

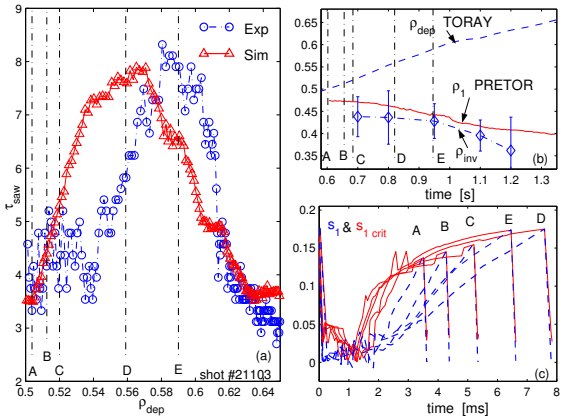

Figure 1. *Experiment and simulation which identify the heating location maximizing* τ_{saw}

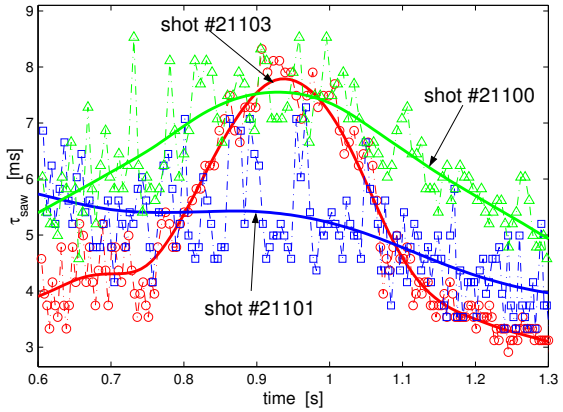

Figure 2. *Experimental traces which show the presence of a heating location destabilizing sawteeth*

profile has a maximum ranging from 8 MW/m^3 at $\rho_{dep} \simeq 0.5$ to 6 MW/m^3 at $\rho_{dep} \simeq 0.65$, with a corresponding deposition width $\Delta\rho_{dep} \simeq 0.08$. The simulation reproduces rather well the variation of the sawtooth period, and provides a location maximizing τ_{saw} (ρ_{max}) which is shifted as compared to the experimental trace by only $\Delta\rho \simeq 0.025$, that is 0.6 cm, below the errorbars on both the TORAY–GA deposition profile and the equilibrium reconstruction.

In Figure 1(b) the barycentre of the TORAY–GA power density profile ρ_{dep} is plotted versus time and compared with the before crash ρ_1 computed by the PRETOR simulation as well as with the experimental inversion radius ρ_{inv}, determined from the soft X–ray (SXR) emissivity profiles. Note that at the time of maximum τ_{saw}, both in the experiment and in the simulation, ρ_{dep} is clearly outside ρ_{inv} and the computed ρ_1, by $\Delta\rho \simeq 0.15$ (more than 3 cm), which is larger than the possible errorbars. Moreover both the PRETOR ρ_1 and the experimental ρ_{inv} have the same behaviour during the power sweep. This shows a general behaviour: ρ_1 moves inward when heating power is deposited outside this surface.

In Figure 1(c) we have plotted the time evolution of the relevant terms determining τ_{saw} in the simulation [7, 8, 9], that is the shear s_1 and the critical shear $s_{1\,\mathrm{crit}}$ at ρ_1. We have chosen 5 sawteeth at five time slices during the simulation. These are identified in Figures 1(a) and 1(b) by dash–dotted vertical lines. The key role in determining τ_{saw} is played by the speed at which s_1 grows up during the sawtooth ramp (for graphical purposes the time quoted in x–axis has been rescaled to zero at the start of each sawtooth).

Although all the plasma parameters of the model are computed at ρ_1, it results that the heating location which most efficiently stabilizes sawteeth is located outside $q = 1$. This is because plasma profiles respond to transport equations, and so a desired effect to be obtained on a given flux surface is not necessarily obtained when heating exactly on that surface. We emphasize also that this heating location does not correspond to any specific physical surface.

In Figure 2 we compare the τ_{saw} time trace of shot ♯21103 with the time traces of shots ♯21101 and ♯21100. These two discharges have been obtained with the same set–up and the same plasma of shot ♯21103, but a fourth ECH beam has been added during the vertical sweep of the other three beams. In the case of shot ♯21101 the fourth beam was aiming at a fixed location just inside ρ_1, whereas in shot ♯21100 the fourth beam was aiming almost at the plasma centre. Only shot ♯21101 does not present a maximum of τ_{saw} around 0.95 s. We deduce that localized heating at the location just inside ρ_1 used in this shot, $\rho_{dep} \simeq 0.35$ ($\rho_{dep} \simeq 75\%\rho_{inv}$) has a destabilizing effect on sawteeth. We have performed a PRETOR simulation looking for this location with the following set–up (Figure 3). The equivalent of three gyrotron beams, 1.35 MW, is deposited at ρ_{max} and we add the sweep of one beam of 0.45 MW along the full minor radius. An experiment of power sweep starting from Ohmic conditions allows us to identify stabilizing heating locations, a sweep performed starting from heating conditions in which τ_{saw} is maximized allows us to explore the existence of destabilizing locations.

The results provided by the model agree with the expectations derived from the previous analysis of the experiments. A destabilizing region between $\rho_{dep} = 0.25$ and 0.42 and a τ_{saw} minimum at $\rho_{dep} = 0.33$ are found. This location is almost coincident with the one experimentally identified in shot ♯21101. When the swept beam crosses ρ_{max} a maximum is obtained, in agreement with the experimental result that τ_{saw} increases with increasing power density [4].

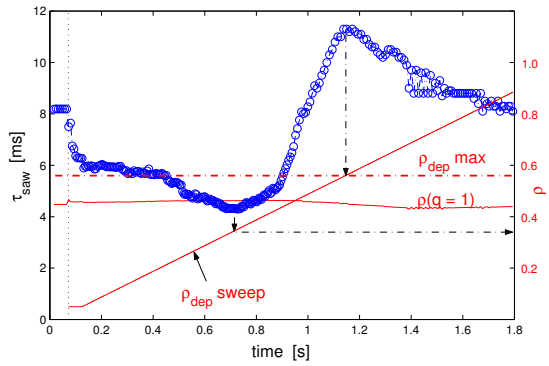

Figure 3. *Simulation which identifies the heating location minimizing τ_{saw}*

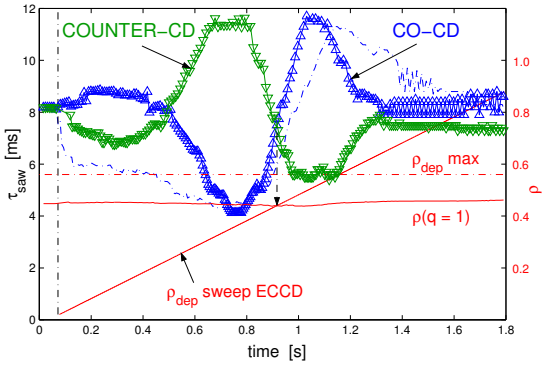

Figure 4. *Simulations showing the effects of co– and counter–CD on τ_{saw}*

The destabilizing effect of localized heating just inside $q = 1$ completely clarifies why maximum stabilisation is obtained when the power is deposited outside $q = 1$ and not exactly on $q = 1$. Since the fraction of the power which is absorbed inside $q = 1$ has a destabilizing effect, the location of ρ_{max} depends on the width of the power density profile, broad profiles providing most efficient stabilisation when ρ_{max} is largely outside $q = 1$ (roughly $\rho_{max} - \rho_1 \simeq 0.5\Delta\rho_{dep}$).

3. Stabilisation and destabilisation with current drive

The same simulation set–up described in the previous section has been used to explore effects due to CD. We keep 1.35 MW of heating power fixed at ρ_{max} and we add the sweep of a small amount of localized CD, 3.5 kA, along the full minor radius (at the plasma centre the local maximum driven current density (0.92 MA/m^2) is about 32% of the local current density, whereas at ρ_1 (0.11 MA/m^2) is less than 4% of the local current density). The results are shown in Figure 4. The τ_{saw} time trace obtained with co–CD (+3.5 kA) is plotted with triangles pointing up, whereas the τ_{saw} time trace obtained with counter–CD (–3.5 kA) with triangles pointing down. When considered alone, that is not accompanied by an amount of heating at the same location, co– and counter–CD have opposite effects at symmetric locations with respect to ρ_1. In particular the stabilizing effect of co–CD and destabilizing effect of counter–CD when applied outside ρ_1 is in agreement with experimental observations in TCV [4]. We observe also that in particular counter–CD has opposite and competitive effects at the same locations as compared with localized heating (Figure 3 and dash–dotted line in Figure 4). Therefore we must expect that in experimental conditions when co–, counter–CD, and localized heating are simultaneously present, very complex time traces can result. JET shot ♯51800 with ICRH and ICCD provides an interesting example in this sense.

4. Analysis of a JET shot with ICRH/ICCD

A set of shots have been performed in JET with ICRH and ICCD at $\omega \approx 2\omega_{cH}$ producing a ramp in B_t and I_p in order to change the ICRF resonance location with respect to ρ_{inv}, while keeping q and ICRF power constant [5]. The time trace of τ_{saw} as well as of the $\omega \approx 2\omega_{cH}$ resonance location and of R_{inv} obtained in shot ♯51800 are shown in Figure 5. We observe that τ_{saw} has a complex behaviour as the resonance moves through the inversion radius, with a sequence of two maxima and minima in the time interval between 23.7 s and 25.5 s.

The different ICRF–related quantities have been computed and analyzed [5] with the codes PION [13] and FIDO [14]. In particular the three–dimensional Monte Carlo code FIDO allows the detailed modelling of the resonating ion distribution and the ICCD density profile, taking into account the effects of finite orbit width and of trapped resonating ions. The collisional electron heating power density and the current density driven by ICRF–accelerated protons as computed by FIDO for shot ♯51800 at 24.5 seconds are shown in Figure 6. The calculated current is dominated by the current of diamagnetic type [15], caused by the large orbit widths of the resonating trapped high–energy protons. Thereby the driven current density profile is bipolar, and the counter– and co–CD components are at shifted locations with respect to the position of the maximum of the collisional heating power density profile. This is particularly interesting since, differently from cases with ECH and ECCD, both counter–CD and co–CD are simulataneously involved and at different locations with respect to the heating power. Note that direct fast particle effects on τ_{saw} are negligible in the time interval we are considering. They become relevant only when the resonance approaches the magnetic axis and are likely to be responsible of the observed increase of τ_{saw} up to 230 ms [5].

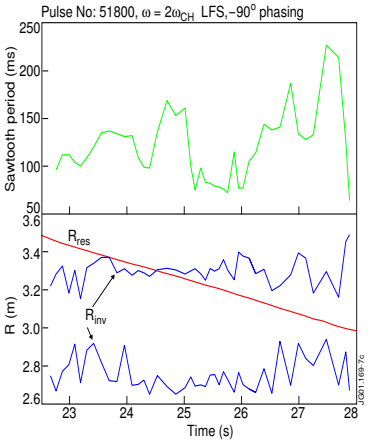

Figure 5.

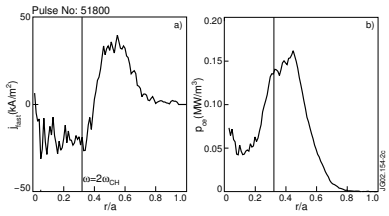

Figure 6. (↑) *ICCD (a) and collisional electron heating power (b) densities at 24.5 s (FIDO results)*

Figure 5. (←) *Time traces of τ_{saw}, of the ICRF resonance and of R_{inv} (JET shot ♯51800)*

Figure 7. (→) *Corresponding simulation in the interval t = 22.5s-26.0s*

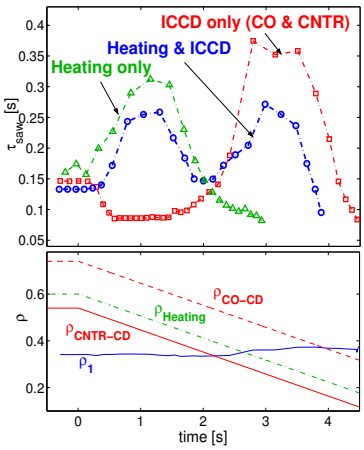

Figure 7.

We have performed simulations of the sawtooth period behaviour of this shot in the mentioned time interval (Figure 7), considering first separately the effects due to electron localized heating (triangles) and due to the co– and counter–ICCD components (squares), and then taking into account both ICRH and ICCD (circles). Time t = 0 s in the simulation corresponds to time t = 22.5 s in the discharge. The profiles of co– and counter–CD as well as the electron heating power density used in the simulation are derived from the results obtained by FIDO for several time slices. The barycentre of these density profiles have been plotted and compared with the time evolution of ρ_1 as obtained in the simulation in which both ICH and ICCD effects have been taken into account (Figure 7). The separate effects due to heating and current drive are consistent with those shown in Figures 3 and 4, and with the related TCV experimental results (Figures 1, 2 and Refs. [3, 4, 9]). The superimposition of these separate effects provides the sequence of maxima and minima observed in the experimental trace of the JET shot.

5. Conclusions

Strong experimental effects due to localized heating and current drive have been identified and explained with the help of transport simulations involving a sawtooth period model. A specific and complex sawtooth period time trace observed in JET in the presence of ICRH and ICCD has been explained and shown consistent with the superimposition of separate effects due to localized heating and current drive as identified by simulations and experiments with ECH/ECCD in TCV.

This work was partly conducted under the European Fusion Development Agreement, and was supported in part by EURATOM and the Swiss National Science Foundation.

References

[1] Sauter O *et al* 2002 *Phys. Rev. Lett.* **88** 105001
[2] Hanada K *et al* 1991 *Phys. Rev. Lett.* **66** 1974
[3] Goodman T P, Henderson M A *et al* 1999 *Proc. 26th EPS Conf. on Control Fusion and Plasma Physics (Maastricht, 1999)* ECA Vol. **23J** 1101
[4] Henderson M A, Goodman T P *et al* 2001 *Fusion Eng. Des.* **53** 241
[5] Mantsinen M J *et al* 2001 *Proc. 28th EPS Conf. on Control. Fusion and Plasma Physics, (Madeira, 2001)*, ECA Vol **25**, P 2.083; submitted to *Plasma Phys. Control. Fusion* (2002)
[6] Boucher D and Rebut P H 1993 *Proc. IAEA Tech. Com. on Advances in Simulation and Modell. of Thermonuclear Plasmas (Montreal, 1992)* p 142
[7] Porcelli F *et al* 1996 *Plasma Phys. Control. Fusion* **38** 2163
[8] Sauter O *et al* 1999 *Theory of Fusion Plasmas (Proc. Joint Varenna–Lausanne Int. Workshop)* Varenna 1998, eds Connor Sindoni Vaclavik, ISPP-18 (Compositori Bologna) 403
[9] Angioni C *et al* 2001 *Theory of Fusion Plasmas (Proc. Joint Varenna–Lausanne Int. Workshop)* Varenna 2000, eds Connor Sauter Sindoni, ISPP-19 (Compositori Bologna) 73
[10] Angioni C *et al* 2002 *Plasma Phys. Control. Fusion* **44** 205
[11] Sillen R M J *et al* 1986 *Nucl. Fusion* **26** 303
[12] Lin-Liu Y R *et al* 1999 *Proc. 26th EPS Conf. on Control Fusion and Plasma Physics (Maastricht, 1999)* ECA Vol. **23J** 1245
[13] Eriksson L-G, Hellsten T, and Willén U 1993 *Nucl. Fusion* **33** 1037
[14] Carlsson J *et al* 1995 *Theory of Fusion Plasmas (Proc. Joint Varenna–Lausanne Int. Workshop)* Varenna 1994, eds Connor Sindoni Vaclavik, ISPP-16 (Compositori Bologna) 351
[15] Hellsten T, Carlsson J, Eriksson L-G 1995 *Phys. Rev. Letters* **74** 3612